Key words: mass spectrometry (MS), protein stability, ligand binding, chloramphenicol acetyltransferase (CAT), collision-induced unfolding (CIU), collision-induced dissociation (CID)

Gas-phase stability and thermodynamics of ligand-bound, binary complexes of chloramphenicol acetyltransferase reveal negative cooperativity

Alexis N. Edwards, Anthony J. Blue, Jessica M. Conforti, Michael S. Cordes, Michael A. Trakselis[#], Elyssia S. Gallagher*

Baylor University, Department of Chemistry and Biochemistry, Waco TX, 76798.

***Corresponding Author**
Baylor University
Department of Chemistry and Biochemistry
Waco TX, 76798
Email: elyssia_gallagher@baylor.edu
ORCID: 0000-0002-5411-7285

[#]Michael A. Trakselis
ORCID: 0000-0001-7054-8475

ABSTRACT: The biological role of the bacterial chloramphenicol (Chl)-resistance enzyme, chloramphenicol acetyltransferase (CAT), has seen renewed interest due to the resurgent use of Chl against multi-drug resistant microbes. This looming threat calls for more rationally designed antibiotic derivatives that have improved antimicrobial properties and reduced toxicity in humans. Herein, we utilize native ion mobility spectrometry – mass spectrometry (IMS-MS) to investigate the gas-phase structure and thermodynamic stability of the type I variant of CAT from *Escherichia coli* (*Ec*CAT_I) and several *Ec*CAT_I:ligand-bound complexes. *Ec*CAT_I readily binds multiple Chl without incurring significant changes to its gas-phase structure or stability. A non-hydrolyzable acetyl-CoA derivative (S-ethyl-CoA, S-Et-CoA) was used to kinetically trap *Ec*CAT_I and Chl in a ternary, ligand-bound state (*Ec*CAT_I:S-Et-CoA:Chl). Using collision-induced unfolding (CIU)-IMS-MS, we find that Chl dissociates from *Ec*CAT_I:S-Et-CoA:Chl complexes at low collision energies, while S-Et-CoA remains bound to *Ec*CAT_I even as protein unfolding occurs. Gas-phase binding constants further suggest that *Ec*CAT_I binds S-Et-CoA more tightly

than Chl. Both ligands exhibit negative cooperativity of subsequent ligand binding in their respective binary complexes. While we observe no significant change in structure or stability to *Ec*CAT$_I$ when bound to either or both ligands, we have elucidated novel gas-phase unfolding and dissociation behavior and provided a foundation for further characterization of alternative substrates and/or inhibitors of *Ec*CAT$_I$.

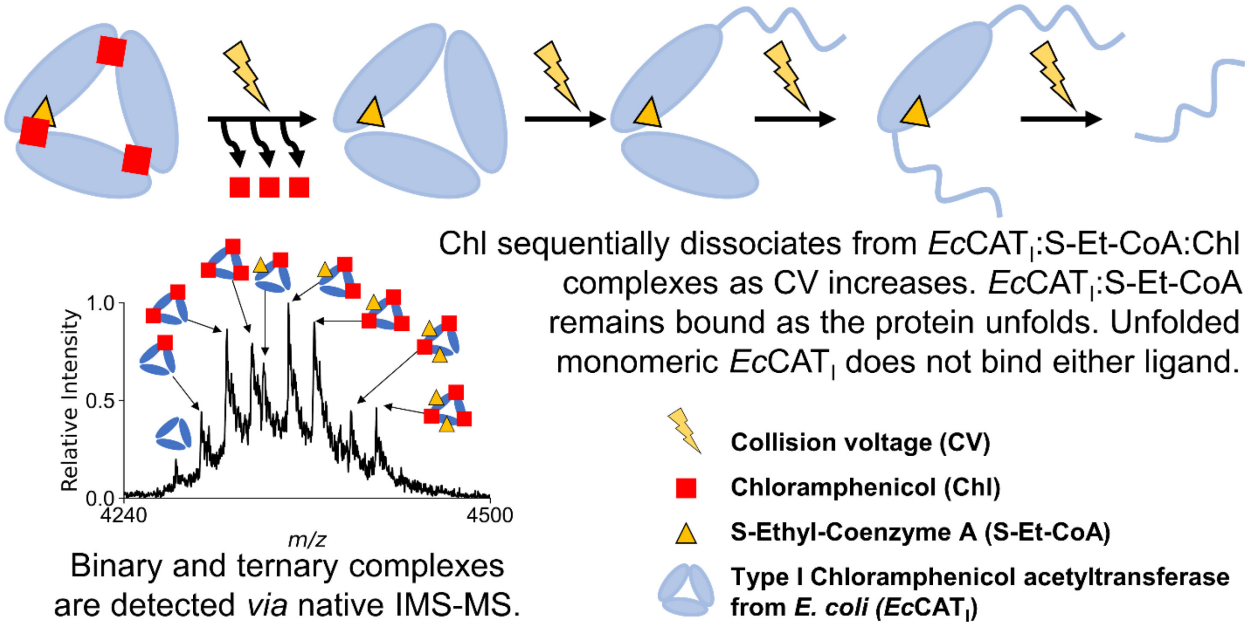

Statements and Declarations: This work was supported by the following funding agencies: Welch Foundation (AA-1899 to E.S.G.), National Science Foundation (CHE-2104242 to M.A.T.), and National Institutes of Health (1R15GM146188-01). The authors declare no competing interests.

INTRODUCTION

Multi-drug resistant (MDR) microbes represent one of the most significant and immediate challenges to global public health. Over 5 million deaths are associated globally with antimicrobial-resistant infections each year [1]. The discovery of antibiotics, almost 100 years ago, immediately transformed modern medicine, leading to a dramatic increase in human life expectancy [2]. However, the overuse and over-prescription of antibiotics has led to the evolution of drug resistance in many bacterial pathogens, creating a crisis of antimicrobial resistance [3].

Antibiotics, including natural products and synthetic analogs, are utilized to inhibit microbial growth and proliferation. Chloramphenicol (Chl), first isolated from *Streptomyces venezuelae* in 1947 and then synthesized in 1949 [4-6], is an aniline-based antibiotic that is employed against a wide spectrum of disease-causing bacteria by inhibiting protein synthesis. This compound was used to treat many microbial infections until 2007, when the WHO classified it as a "probable human carcinogen" and it was phased out of use [7]. However, Chl is still widely used in the management and treatment of superficial eye infections [8]. A study in India determined a 90-95% re-emergence of Chl susceptibility in *Salmonella enterica* [9], which led to a resurgence in the use of Chl in less-developed countries as a cost effective option to treat MDR microbial infections [10, 11]. Given the continued use and re-popularization of the drug, there has been a renewed push to design less harmful derivatives of Chl to address the ever-growing threat of MDR microbes [12].

Chl's mechanism of action is based on its covalent binding to the A-site of the 50S ribosomal subunit; blocking incoming tRNA and preventing peptide-bond formation, which effectively prevents translation of new proteins, leading to cell cycle arrest or cell death [13]. Microbial resistance to Chl is conferred by a gene for chloramphenicol acetyltransferase (CAT) and is one of the most widespread genetic elements, functionally viable in plants, animals, and bacteria [14]. CAT inactivates Chl by one or two acetylations, donated from acetyl-coenzyme A (Ac-CoA) [15, 16]. This catalytic transfer first targets the C3-hydroxyl of Chl, which is sufficient to prevent Chl-ribosome binding. In the presence of excess Ac-CoA, a second acetylation can occur after a non-enzymatic acetyl transfer from the C3-hydroxyl to the C1-hydroxyl of Chl. This internal rearrangement results in the original C3-hydroxyl being available for a second catalytic transfer from excess Ac-CoA, resulting in di-acetylated Chl (**Fig. 1**) [17, 18].

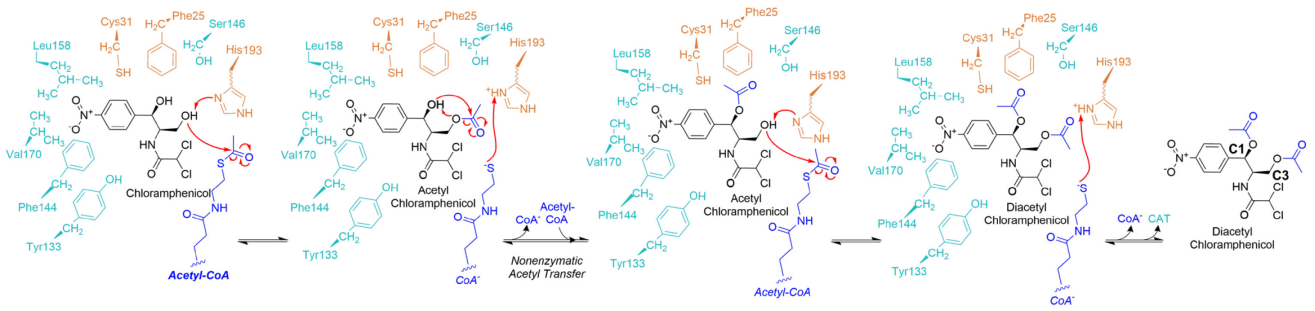

Fig. 1 Mechanism of *Ec*CAT$_I$, causing acetylation and inactivation of Chl. Chl (black) bound in the active site of trimeric *Ec*CAT$_I$ (teal and orange, highlighting the contributing amino acids from two different *Ec*CAT$_I$ monomers), is acetylated at the C3-OH from acetyl-CoA (blue). Afterwards, a non-enzymatic acetyl transfer occurs from C3-OH to C1-OH, enabling a second acetylation at the C3-OH to yield the di-acylated Chl. Figure adapted from reference [47].

CAT enzymes come in several different isoforms from a wide variety of organisms and have been used in clinical and industrial applications [19-23]. CATs from *Escherichia coli* have three unique isoforms (*Ec*CAT$_I$, *Ec*CAT$_{II}$, and *Ec*CAT$_{III}$) that can form both homotrimers and heterotrimers with the other two isoforms. *Ec*CAT$_{III}$ is the most well studied CAT variant, as its crystal structure was solved first [24], and it was utilized as a model protein system to study folding and thermodynamic stability [25]. There has been recent interest in the thermodynamic stability and substrate promiscuity of *Ec*CAT$_{III}$, allowing for mesophilic catalysis of different esters, such as isobutyl isobutyrate and perillyl alcohol [19, 20]. Mutagenesis to enlarge the active site of CAT to allow for larger substrates has been utilized to expand industrial relevance [21]. *Ec*CAT$_I$ is the most predominant isoform and is commonly used in recombinant protein expression as a selection marker to screen bacterial transformants; *e.g.,* it is employed in BL21(DE3) *E. coli* as a component of the pRARE and pLys series of plasmids [26].

The looming threat of MDR microbes and the revival of Chl use calls for a detailed study of the structure-function relationship that contributes to CAT's thermodynamic stability and protein-ligand interactions. Native mass spectrometry (MS) is a gas-phase technique that is used for structural analysis of intact protein and protein complexes by preparing samples in native-like conditions and then transferring them from solution to the gas-phase via a soft ionization technique, such as electrospray ionization (ESI). This approach maintains noncovalent interactions within the protein, and with bound ligands, as they transition into the gas-phase, allowing for determination of stoichiometry, composition, subunit interactions, reaction intermediates, and binding affinities [27-32]. Ion mobility spectrometry (IMS), often paired with native MS, allows for determination of protein mobilities through a drift gas under the influence of an electric field. This mobility can then be related to a protein or complex's three-dimensional structure, resulting in an average momentum transfer cross section (colloquially referred to as

collision cross section, CCS) [33-35]. Two additional gas-phase techniques, known as collision-induced unfolding (CIU) and collision-induced dissociation (CID), utilize the stepwise increase of collision voltage (CV) to induce structural changes via unfolding or complex dissociation, causing a change in mobility or loss of signal for the target analyte, respectively [36-38]. Together, these techniques allow for the in-depth investigation of the distributions of size, shape, stability, and binding behavior of proteins and protein-ligand complexes.

Herein, we utilized native MS paired with IMS to investigate the gas-phase structures of *Ec*CAT_I, complexed with Chl and/or a CoA derivative (S-ethyl-CoA, S-Et-CoA), to examine the impact of these ligands on the stability and thermodynamics of the binary and ternary enzyme complexes. *Ec*CAT_I binds multiple Chl or S-Et-CoA in the gas-phase without experiencing structural or stability changes. Incubation of *Ec*CAT_I, Chl, and S-Et-CoA results in formation of stable ternary complexes (*Ec*CAT_I:S-Et-CoA:Chl), where Chl is more readily lost as CV increases. Because of the ability to simultaneously quantify individual species using native MS, both Chl and S-Et-CoA were found to bind with negative cooperativity to *Ec*CAT_I. Importantly, this work characterized the thermodynamic binding parameters and cooperativity of binary *Ec*CAT_I enzyme complexes in the gas-phase that aligns with previous solution-phase behavior [39], highlighting the utility of native MS for quantifying ligand-bound enzyme complexes. Furthermore, this work indicates that native IMS-MS may be a valuable tool for the discovery and characterization of novel inhibitors

MATERIALS AND METHODS

Materials.

Lyophilized cytochrome *c*, ubiquitin, myoglobin, thyroglobulin, ferritin, catalase, conalbumin, vitamin B12, chloramphenicol, CoA, acetyl-CoA, and isopropyl ß-D-1-thiogalactopyranoside (IPTG) were from Sigma Aldrich (St. Louis, MO). S-ethyl-CoA was from Jena Bioscience (Jena, Germany). Ammonium acetate and formic acid were from VWR International (Radnor, PA). Methanol and Pall 10K MWCO spin filters were from Thermo Fisher Scientific (Waltham, MA). Nanopure water was obtained from a Purelab Flex 3 water purification system (Elga, Veolia Environment S. A., Paris, France).

Cloning and protein purification of EcCAT_I.

EcCAT_I was expressed from the pRARE plasmid with 0.3 mM IPTG in Rosetta2 BL21 DE3 cells (MilliporeSigma, Burlington, MA), grown in LB media containing 20 μg/mL chloramphenicol for 12 hours at 37 °C. The cells were pelleted and resuspended in buffer A (20 mM Tris-HCl pH 7.5, 100 mM NaCl, 1 mM EDTA, 5 mM β-mercaptoethanol). The resuspension was incubated at 4 °C with 0.5 mg/mL lysozyme for 1 hour, sonicated, and then heat treated at 70 °C for 30 minutes. The supernatant was collected after centrifuging for 40 min at 52,000 x g using an Avanti J-26 XP (Beckman Coultier, Pasadina, CA) to remove the insoluble material. The clarified sample was then loaded onto an HiTrap Q HP column equilibrated with Buffer A and eluted with a linear gradient starting with 100 % Buffer A and transitioning to 100% Buffer B (Buffer A with 2 M NaCl) over 30 minutes using an AKTA Pure FPLC (Cytiva, Marlborough, MA). *Ec*CAT_I-containing fractions were pooled, concentrated, and loaded onto a Superdex 200 gel filtration column equilibrated with Buffer A and 10% glycerol. The size exclusion column was calibrated with protein standards, including: thyroglobulin (669 kDa), ferritin (440 kDa), catalase (250 kDa), conalbumin (75 kDa), myoglobin (17.6 kDa), and vitamin B12 (1.3 kDa) prior to the run. *Ec*CAT_I-containing fractions were then pooled, concentrated with a 10K MWCO spin filter, and quantified using a UV-Vis (ε = 12,660 M^{-1} cm^{-1}) before flash freezing in liquid N_2 and storing at -80 °C. The *Ec*CAT_I protein identity was validated using bottom-up proteomics (see electronic supplementary material, **Fig. S1**).

Sample preparation for Native MS analysis.

Denatured samples, used for IMS calibration, were prepared at 5 μM - 10 μM in 49:49:2 (v/v/v) methanol: water: formic acid. Native samples (10 μM final concentration) were buffer exchanged and desalted in 200 mM ammonium acetate pH ~7.0, unless otherwise stated, using micro-spin P-6 gel columns (Bio-Rad Laboratories, Mississauga, ON) followed by concentration on Pierce 10K MWCO concentrator columns. For protein-ligand binding experiments, the proteins were desalted as stated above before being mixed with ligands, which were prepared in 200 mM ammonium acetate immediately prior to complex formation. While the ratio of protein:ligand varied depending on the ligand (see Results and electronic supplementary material, **Table S1**), the final concentration of *Ec*CAT_I for all experiments was ~10 μM.

Native IMS-MS analysis.

Samples were introduced via open source to a quadrupole-ion mobility-time-of-flight mass spectrometer (Synapt G2-S High-Definition MS, Waters Corporation, Millford, MA). For direct infusion, approximately 5 μL of

sample was loaded into glass capillaries (inner diameter ~1 μm, Sutter), which were pulled using a P-1000 micropipette puller (Sutter Instrument Company, Novato, CA). Instrument parameters were optimized to maintain the native structure of the protein and protein-ligand complexes. The traveling-wave ion mobility cell (filled with N_2) was operated at ~2.07 mbar, with the DC voltage waves set to either 15 V, 17 V, or 20 V and the traveling wave height at 250 m/s. For additional information, see electronic supplementary material, **Table S2**. The instrument contained N_2 gas in the IMS cell, He gas in the helium cell, and Ar gas in the trap and transfer cells.

Denatured calibrants were run between trials of native samples. For both denatured and native samples, each mass spectrum was averaged over a one-, three-, or five-minute acquisition and charge states were calculated by hand to confirm oligomeric states. Replicate trials were consistent across multiple days. IMS and CIU were used to confirm detected oligomeric states and their stability. The IMS cell was primarily filled with N_2, but the calibrant CCS values were determined using drift tube (DT)-IMS filled with He. Therefore, following recommendations from Gabelica *et. al* [40], experimentally determined CCS are labeled $^{TW}CCS_{N2\rightarrow He}$, where the subscript indicates that the experimental CCS were measured in N_2 and the calibrant CCS were determined in He. The superscript identifies the type of IMS (traveling wave, TW) used for the measurements. $^{TW}CCS_{N2\rightarrow He}$ calibration curves were generated using a previously described protocol [41] as were the corresponding uncertainties [42]. CIU was performed by increasing the trap-cell collision voltage (CV) from 0 V to 100 V in 5 V increments. Rather than using the quadrupole to isolate each individual charge state prior to CIU experiments, unfolding of all charge states (all ion unfolding) [43] was done. Each charge state was then independently analyzed. The percent survival of individual species were plotted and fit using Prism 9.5 (GraphPad, San Diego CA). If the signal-to-noise ratio (S/N) of an analyte was less than 3, that peak was not used for IMS or CIU analysis and was omitted from structural characterization, thermodynamic calculations, and binding quantification.

Simulated CCS calculations of EcCAT$_I$.

MD simulations used GROMACS 2022.3 [44] with the CHARMM36 forcefield [45] to model gas-phase protein compaction [46]. Initial protein structures were obtained from the Protein Data Bank (PDB), consisting of trimeric apo-*Ec*CAT$_I$ (PDB: 1PD5) and *Ec*CAT$_I$ bound to Chl (PDB: 3U9F) [47]. Protonation sites were predicted using a charge-prediction algorithm within the Collidoscope package [48] for the 21+ charge state of both the trimeric *Ec*CAT$_1$ and *Ec*CAT$_1$:3Chl complexes. The charged protein complexes (with or without Chl) underwent an MD relaxation for 5 ns based on a protocol adopted from Rolland *et. al* [46]. Briefly, the protein is relaxed in an

explicit water solvent box for 1 ns, after which all water molecules are deleted. Following this deletion, the protein ion is subjected to a 5 ns production run in vacuum. CCS predictions of the post-MD protein structures used Collidoscope, which is based on the trajectory method [49] for predicting CCS, with He as the buffer gas. $^{TM}CCS_{He}$ indicates that CCS predictions used the trajectory method (TM, superscript) and He buffer gas (subscript). Ten replicates were performed for both the trimeric apo-*Ec*CAT_1 and *Ec*CAT_1:3Chl complexes to predict the $^{TM}CCS_{He}$. Replicates started from the same PDB structures but underwent different charge-site assignment and MD relaxation prior to $^{TM}CCS_{He}$ prediction. Data is presented as the average ± standard deviation.

Direct ESI-MS binding measurements.

To quantify binding between *Ec*CAT_1 and ligands of interest, either Chl or S-Et-CoA, direct ESI-MS binding measurements were conducted, following the protocol published by Baez Bolivar *et al.* [50]. To summarize, stepwise binding of a ligand (L) to a protein complex (P) containing three binding sites can be described using equation 1, with the corresponding mass balance equations being described with equations 2 and 3:

$$P + L \rightleftharpoons PL + L \rightleftharpoons PL_2 + L \rightleftharpoons PL_3 \qquad (1)$$

$$[L]_0 = [L] + [PL] + 2[PL_2] + 3[PL_3] \qquad (2)$$

$$[P]_0 = [P] + [PL] + [PL_2] + [PL_3] \qquad (3)$$

where $[L]_0$ is the initial concentration of the ligand of interest and $[P]_0$ is the initial concentration of the trimeric protein complex, *Ec*CAT_1. The abundance ratio (R_i, where *i* is the number of ligands in the binary complex) of ligand-bound protein (PL) to free protein (P) can then be described as:

$$R_i = \frac{Ab(PL)_i}{AB(P)} = \frac{[PL]_i}{[P]} \qquad (4)$$

Baez Bolivar *et al.* utilized a high-resolution Orbitrap to complete their experiments, allowing for the abundance of each species to be used for calculating R_i [50]. A lower resolution instrument was used here (Waters Synapt G2-S); therefore, the area under each peak was integrated using MassLynx and peak area was used to determine R_i values. Briefly, the area under each charge-state peak was determined using the integrate function in the spectrum window (Process→Integrate) of MassLynx. The following values were used for integration: join valleys if peaks resolved to 1.00% above baseline, reduce peak tailing until trailing edge is no more than 10% wider than leading edge, raise

baseline by no more than 5.00% of peak height, detect shoulder peaks not selected. The following parameter was changed periodically to ensure that the start and stop *m/z* value for each replicate was comparable: draw vertical if peak resolved to #% above baseline.

The fraction of ligand-occupied binding sites (F_s) for a protein containing three binding sites, quantified based on the (R_i), is defined by equation 5:

$$F_s = \frac{\sum iR_i}{3(1+\sum R_i)} \qquad (5)$$

Using R_i, F_s, $[L]_0$, and $[P]_0$, the apparent dissociation constant ($K_{d,i}$) of sequential ligand binding was calculated. $K_{d,i}$ for sequential binding of L can be defined by:

$$K_{d,1} = \frac{[L]_0 - 3F_s[P]_0}{R_1} \qquad (6)$$

$$K_{d,2} = \frac{[L]_0 - 3F_s[P]_0}{\frac{R_2}{R_1}} \qquad (7)$$

$$K_{d,3} = \frac{[L]_0 - 3F_s[P]_0}{\frac{R_3}{R_2}} \qquad (8)$$

We assume the binding sites are equivalent but exhibit cooperativity due to the $K_{d,i}$ increasing as the number of bound ligands increases. Therefore, we calculated an intrinsic dissociation constant ($K_{d,\mathrm{intrin}}$) and corresponding cooperativity factors (α and β). Because negative cooperativity was observed, the intrinsic dissociation constant ($K_{d,\mathrm{intrin}}$) is defined by equation 9:

$$3K_{d,1} = \frac{1}{\alpha}K_{d,2} = \frac{1}{3\beta}K_{d,3} = K_{d,\mathrm{intrin}} \qquad (9)$$

where α and β are cooperativity factors when a second or third ligand binds, respectively.

Data Analysis.

Data analysis was completed using the following programs: Protein Metrics PMi-Byonic (v3.6.0), MassLynx (v.4.2), and CIUSuite 2 [38]. Two-tailed F-tests and *t* tests, at the 95% confidence interval, were used to determine statistical significance. To calculate CIU50 values, the following parameters in CIUSuite 2 were used: minimum feature length (steps) = 2, feature allowed width (drift axis units) = 1, and maximum CV gap length (CV

steps) = 1. CID50 values were calculated as follows: the intensity for each individual peak was recorded at each CV step. The CID50 was identified between CV steps in which the signal intensity decreased by 50%.

RESULTS

Trimeric Ec*CAT$_I$ binds multiple Chl in the gas-phase.*

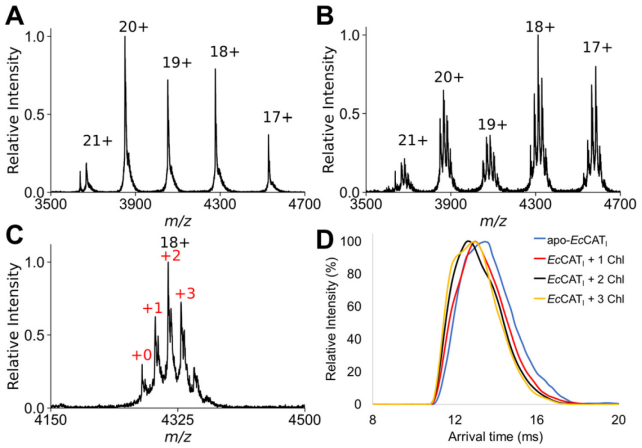

Fig. 2: Analysis of gas-phase native-like *Ec*CAT$_I$. Under native conditions, *Ec*CAT$_I$ forms a homotrimer with multiple charge states (**A**) that can bind multiple Chl (**B** and **C**) without experiencing a change in arrival time (**D**). Charge states and number of bound Chl are indicated in black and red text, respectively.

CAT readily forms homo- or hetero-trimers in solution [51], dependent on the CAT variant. When sprayed under native-like conditions, a homotrimer (MW 76,990 ± 10 Da) with charges ranging between 17+ and 21+ is detected (**Fig. 2A**). The masses for each isoform of *Ec*CAT$_I$, *Ec*CAT$_{II}$, and *Ec*CAT$_{III}$ are 25,663 Da [52], 24,778 Da [53], and 24,994 Da [54], respectively. Our experimental molecular weight, in conjunction with bottom-up proteomics experiments (see electronic supplementary material, **Fig. S1**), confirms that only the *Ec*CAT$_I$ isoform was present in our samples, supporting that the trimeric species is in fact a homotrimer. For each charge state, a single, broad arrival time is observed (see electronic supplementary material, **Fig. S2**). Depending on the charge state, the gas-phase $^{TW}CCS_{N2\rightarrow He}$ values for native-like *Ec*CAT$_I$ are 4100 ± 130 Å^2 to 5000 ± 110 Å^2 (**Table 1**). This is consistent with simulated gas-phase $^{TM}CCS_{He}$ values for the 21+ charge state (4890 ± 70 Å^2, PDB: 1PD5).

The *Ec*CAT$_I$ trimer contains three interfacial active sites between monomer subunits, allowing for the binding of up to three Chl [47]. When *Ec*CAT$_I$ was incubated with Chl, a distribution of one, two, or three Chl were detected for each trimeric-protein charge state (**Fig. 2B and 2C**). Regardless of the number of Chl bound to the *Ec*CAT$_I$ trimer, there was no significant change in arrival time (**Fig. 2D**), suggesting that there is no significant change in the three-dimensional structure of the complex. This is consistent with simulated gas-phase $^{TM}CCS_{He}$ values for the 21+ charge state when bound to 3 Chl (4740 ± 40 Å^2, PDB: 3U9F).

Trimeric* Ec*CAT*$_I$ *undergoes two unfolding events independent of Chl.

When increasing collisional voltage (CV) is applied to the trap cell, trimeric *Ec*CAT$_I$ regularly undergoes two discrete unfolding events (**Fig. 3** and electronic supplementary material, **Fig. S3**), as indicated by the increases in arrival time. For each charge state, the two distinct unfolding events result in a significant increase in $^{TW}CCS_{N2\rightarrow He}$, determined at the 95% confidence interval (**Table 1**). Unfolding patterns were quantified using CIU50, which represents the CV at which 50% of a compact protein transitions to a more extended state due to unfolding. The 18+ charge state of trimeric *Ec*CAT$_I$ initially unfolds at (42 ± 2) V, followed by a second unfolding event at (49 ± 3) V (**Fig. 3 and** electronic supplementary material, **Table S3**). All other charge states exhibit similar unfolding patterns, though the voltage at which the two unfolding events occur generally decreases with increasing protein charge (see electronic supplementary material, **Fig. S3 and Table S3**).

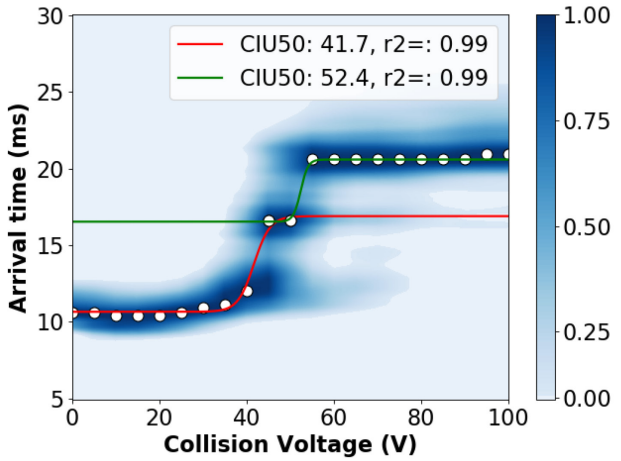

Fig. 3: Trimeric *Ec*CAT$_I$ experiences two distinct unfolding events. The CIU fingerprint for 18+ *Ec*CAT$_I$ shows three distinct arrival times, resulting from the native protein experiencing two unfolding events as CV increases.

Table 1: Collision cross sections ($^{TW}CCS_{N2\rightarrow He}$)[a] representing intact trimeric *Ec*CAT$_I$ at various charge states.

z	Native[b] $^{TW}CCS_{N2\rightarrow He}$, Å^2	Intermediate[b] $^{TW}CCS_{N2\rightarrow He}$, Å^2	Unfolded[b] $^{TW}CCS_{N2\rightarrow He}$, Å^2
17+	4100 ± 130	5800 ± 200	6600 ± 250
18+	4400 ± 180	4900 ± 170	6700 ± 250
19+	4500 ± 160	5000 ± 200	6900 ± 260
20+	4800 ± 130	6800 ± 200	7300 ± 280
21+	5000 ± 110	5800 ± 200	7600 ± 290

[a]Data represents average ± propagated uncertainty (see Edwards et al. [42]).
[b] $^{TW}CCS_{N2\rightarrow He}$ before increasing CV (native), after the first unfolding event (intermediate), and after the second unfolding event (unfolded). Unfolding can be observed in Figs. 3 and S3.

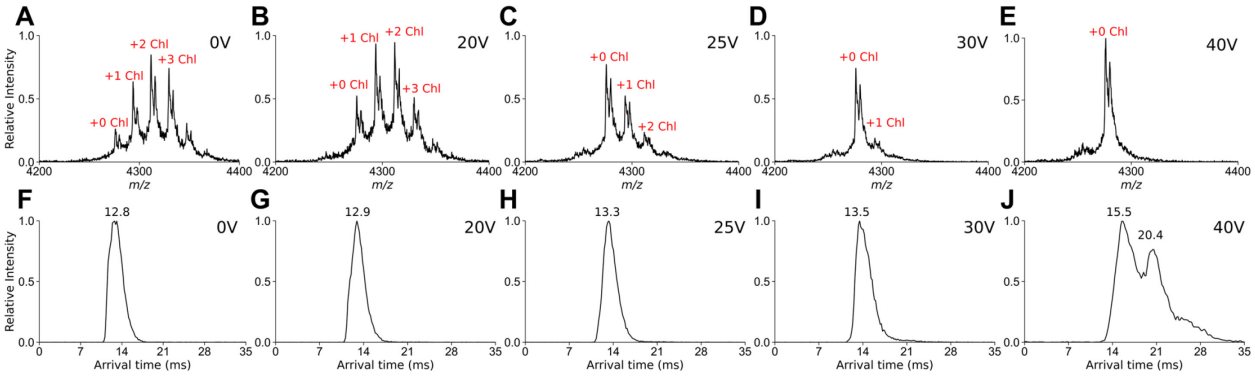

Fig. 4: *Ec*CAT$_I$:Chl remains structurally stable until all Chl dissociates. (**A-E**) As CV is steadily increased from 0 V to 40 V, the most intense species in the mass spectra shift from *Ec*CAT$_I$:2Chl (**A**) to *Ec*CAT$_I$ (**E**), indictive of the gradual loss of Chl. (**F-I**) The protein remains folded as CV increases, even as Chl sequentially dissociates from the complex. After all Chl dissociates from trimeric *Ec*CAT$_I$, the protein experiences its first unfolding event (**J**). Mass spectra and corresponding mobiligrams are for 18+ *Ec*CAT$_I$. Data in the mobiligrams (**F-J**) is integrated for all species shown in the associated mass spectrum (**A-E**), including apo-*Ec*CAT$_I$ and all *Ec*CAT$_I$:Chl complexes.

When *Ec*CAT$_I$:Chl complexes are exposed to increasing CV, Chl sequentially dissociates from the *Ec*CAT$_I$:Chl complex at lower CV than the first unfolding event for apo-*Ec*CAT$_I$. At 0 V, the *Ec*CAT$_I$:2Chl complex is the most intense species (**Fig. 4A)**, but upon increasing voltage between 20 V to 40 V (**Fig. 4B-4E)**, there is a successive loss of bound Chl molecules until only trimeric *Ec*CAT$_I$ remains (**Fig. 4D-E)**. The trimeric CAT does not experience an increase in arrival time until after all Chl dissociates (**Fig. 4F-J**). Because none of the *Ec*CAT$_I$:Chl complexes unfold prior to Chl dissociation, we calculate a CID50 rather than a CIU50 [55, 56]. This CID50 reflects the CV at which 50% of the signal for the complex is depleted due to dissociation of Chl. The CID50 varies for each charge state and for the number of bound Chl, but for all cases, all Chl dissociate by 35 V **(see** electronic supplementary material, **Table S4)**, which is lower than any of the CIU50 values for apo-*Ec*CAT$_I$ **(Table S3)**. Once all Chl has dissociated **(Table S4)**, the *Ec*CAT$_I$ trimer begins its first unfolding event between 30 V and 40 V, as shown in the increase in arrival time compared to the initial arrival time (**Fig. 4F and 4J**). Similar to **Fig. 3**, the 18+

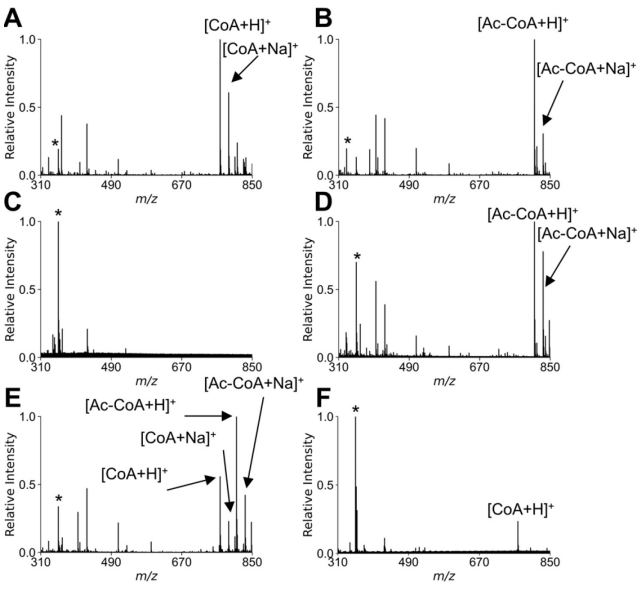

Fig. 5: *Ec*CAT$_I$ readily hydrolyzes Ac-CoA as detected by MS. Mass spectra for CoA (**A**), Ac-CoA (**B**), Chl (**C**), and Ac-CoA:Chl (**D**). *Ec*CAT$_I$ readily hydrolyzes Ac-CoA to form CoA in the absence (**E**) or presence (**F**) of Chl. *denotes a contaminant.

charge state of apo-*Ec*CAT$_I$ experiences a second unfolding event as CV is increased.

Ac-CoA is hydrolyzed by EcCAT$_I$, even in the absence of Chl.

To determine the stability of *Ec*CAT$_I$ as it interacts with Ac-CoA and Chl in a ternary complex, we first investigated whether Ac-CoA or CoA interact with Chl in the absence of *Ec*CAT$_I$ (**Fig. 5**). To highlight the behavior of these molecules with low molecular weight, the x-axis for **Fig. 5** has been adjusted to encompass only low *m/z* values. When sprayed, CoA readily protonates, $[CoA+H]^+$, or forms adducts with sodium, $[CoA+Na]^+$, though the protonated species is the most intense peak (**Fig. 5A**). For Ac-CoA, protonation, $[Ac\text{-}CoA+H]^+$, is again the most intense peak (**Fig. 5B**). Chl was also sprayed alone but was not detected as either a protonated or sodium-adducted ion (**Fig. 5C**). However, when analyzed in negative-ion mode, deprotonated Chl, $[Chl\text{-}H]^-$ was detected (see electronic supplementary material, **Fig. S5**). When Ac-CoA and Chl are incubated together, there is no conversion to CoA or Ac-CoA:Chl complex formation, as the detected peak patterns are similar to experiments analyzing the individual components (compare **Fig. 5D** with **5B**). Additionally, neither acetyl-Chl nor diacetyl-Chl were detected in positive- or negative-ion mode (see electronic supplementary material, **Fig. S5C** and **S5D**). Conversely, when *Ec*CAT$_I$ and Ac-CoA are incubated in a 1:2 molar ratio (*Ec*CAT$_I$:Ac-CoA), a fraction of Ac-CoA is converted to CoA, as evident by the presence of $[CoA+H]^+$ and $[CoA+Na]^+$ (**Fig. 5E**). This change in signal indicates that *Ec*CAT$_I$ hydrolyzes a limited amount Ac-CoA in the absence of Chl,

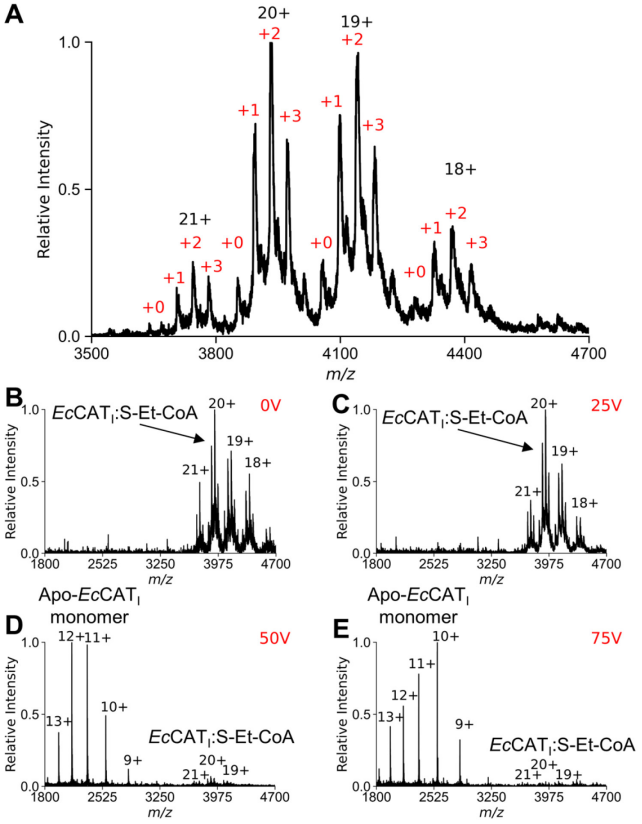

Fig. 6: *Ec*CAT$_I$ coordinates with S-Et-CoA to form a range of *Ec*CAT$_I$:S-Et-CoA complexes. Representative spectrum showing up to three S-Et-CoA bound to *Ec*CAT$_I$ (**A**, x-axis from 3500 *m/z* to 4700 *m/z* to highlight the number of bound S-Et-CoA). (**B-E**) As CV is increased from 0 V to 75 V, the signal intensity for trimeric *Ec*CAT$_I$:S-Et-CoA complexes decreases but does not disappear, suggesting that the binary complex remains intact. (**D-E**) Dissociated apo-*Ec*CAT$_I$ monomers (charge states 9+ to 13+) become the most prominent species at high CV, with binary *Ec*CAT$_I$:S-Et-CoA complexes detected at lower intensity. Charge states and number of bound S-Et-CoA are indicated in black and red text, respectively.

as observed previously for kinetic enzymatic measurements [17]. Binary *Ec*CAT$_I$:Ac-CoA complexes were not observed (see electronic supplementary material, **Fig. S6A**). When *Ec*CAT$_I$ is incubated with Ac-CoA and Chl, at a 1:2.5:2.5 molar ratio (*Ec*CAT$_I$:Ac-CoA:Chl) for 10 minutes prior to analysis, the signal for Ac-CoA is converted to $[CoA+H]^+$ (**Fig. 5F**). Even when the preincubation time was decreased to 1-minute prior to MS analysis, there was no remaining Ac-CoA detected, indicating that *Ec*CAT$_I$ rapidly acetylates Chl and releases products, CoA and acetyl-Chl (not detected). Interestingly, once all Ac-CoA is converted to CoA, some *Ec*CAT$_I$:Chl complexes remain (see electronic supplementary material, **Fig. S6B)**, although the number of Chl bound is fewer than when only *Ec*CAT$_I$ and Chl are incubated together (see electronic supplementary material, **Fig. S6C**)**.**

EcCAT$_I$ coordinates with S-Et-CoA and Chl to form ternary complexes.

Because *Ec*CAT$_I$ deacetylates Ac-CoA in both the absence and presence of Chl, a derivative of CoA lacking the terminal acetyl oxygen, S-Et-CoA (see electronic supplementary material, **Fig. S4D**), was utilized to trap the bound ternary complex (*Ec*CAT$_I$:S-Et-CoA:Chl) to investigate coordination between the protein and ligands. First, we investigated the coordination between *Ec*CAT$_I$ and S-Et-CoA. At a molar ratio of 1:3 (*Ec*CAT$_I$:S-Et-CoA), up to three S-Et-CoA stably coordinate to trimeric *Ec*CAT$_I$ (**Fig. 6A**). Interestingly, and unlike with Chl, the S-Et-CoA remains bound to *Ec*CAT$_I$ as CV increases towards 75 V (**Fig. 6B-6E** and electronic supplementary material, **Fig. S7**). The *Ec*CAT$_I$:S-Et-CoA complexes remain bound at CV of 50 V and 75 V, though unfolded monomeric apo-*Ec*CAT$_I$ (charge states of 9+ to 13+) becomes the most prominent species (**Fig. 6D and 6E**). Because the binary

*Ec*CAT$_I$:S-Et-CoA complexes remain intact as the protein unfolds, unlike binary *Ec*CAT$_I$:Chl complexes, CIU50 values can be determined (see electronic supplementary material, **Fig. S7 and Table S5**). There is no significant difference between the CIU50 values of apo-*Ec*CAT$_I$ and the *Ec*CAT$_I$:S-Et-CoA complexes (see electronic supplementary material, **Fig. S7 and Tables S3 and S5)**, indicating that CoA derivatives do not provide increased stability to the trimeric protein.

When *Ec*CAT$_I$ is incubated with S-Et-CoA and Chl at a ratio of 1:3:3 (*Ec*CAT$_I$:S-Et-CoA:Chl), a distribution of complexes forms, one of which includes trimeric *Ec*CAT$_I$, a single S-Et-CoA, and three Chl (*Ec*CAT$_I$:1S-Et-CoA:3Chl) **(see** electronic supplementary material, **Fig. S8)**. At low CV, species containing Chl (*Ec*CAT$_I$:1Chl, *Ec*CAT$_I$:2Chl, *Ec*CAT$_I$:3Chl, *Ec*CAT$_I$:1S-Et-CoA:1Chl, *Ec*CAT$_I$:1S-Et-CoA:2Chl, and *Ec*CAT$_I$:1S-Et-CoA:3Chl) are the most prominent species, existing at similar intensities (**Fig. 7A and 7B**). As CV is increased (up to 35 V), Chl steadily dissociates from all Chl-containing species **(Fig. 7A and 7B)**, ultimately leaving the more stable *Ec*CAT$_I$:S-Et-CoA complexes intact (**Fig. 7A and 7C)**. As the CV is increased above 40 V, *Ec*CAT$_I$:S-Et-CoA complexes remain bound while experiencing unfolding (**Fig. 7A and 7C and** electronic

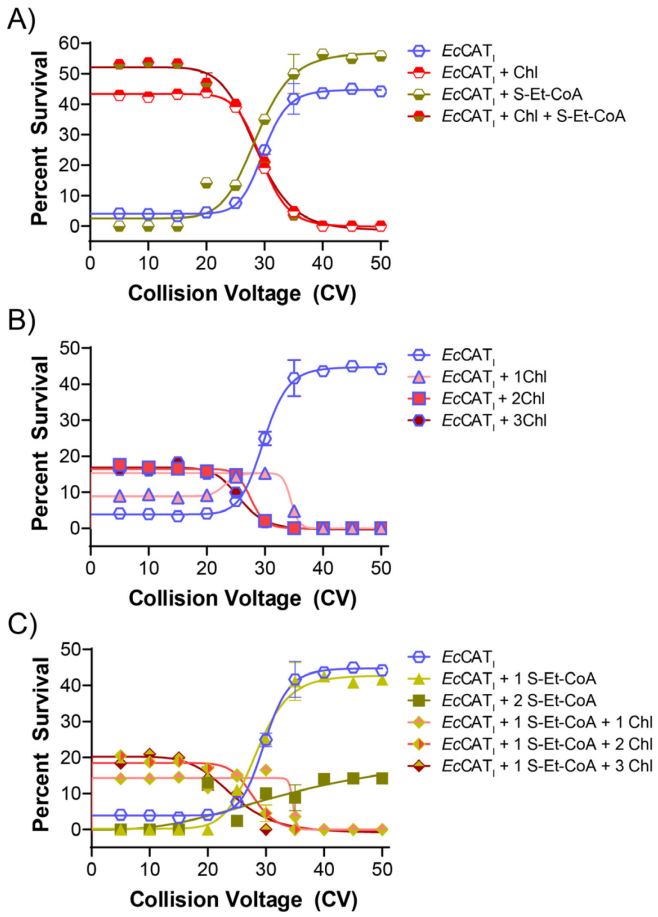

Fig. 7: CID is used to monitor the stability of the ternary *Ec*CAT$_I$ complexes. To simplify interpretation, data is split across three graphs. (**A**) As CV increases, Chl dissociates from *Ec*CAT$_I$:XChl (top red, ⬡) and *Ec*CAT$_I$:XS-Et-CoA:XChl (top red, bottom olive, ⬡) complexes, converting to more thermodynamically stable *Ec*CAT$_I$ (open blue, ⬡) and *Ec*CAT$_I$:XS-Et-CoA (bottom olive, ⬡) complexes, respectively. X indicates any number of bound ligands. (**B**) *Ec*CAT$_I$:XChl complexes with 1 (salmon, △), 2 (red, □), or 3 (maroon, ⬡) Chls are converted to *Ec*CAT$_I$ (open blue, ⬡) with increasing CV. (**C**) Ternary complexes of *Ec*CAT$_I$:1S-Et-CoA:XChl with 1 (top salmon, bottom olive, ◇), 2 (right red, left olive, ◇), or 3 (bottom marron, top olive, ◇) Chl lose Chl as CV increases. Binary complexes of *Ec*CAT$_I$:XS-Et-CoA with 1 (light olive, △) or 2 (dark olive, □) S-Et-CoA increase in abundance as Chl is removed from ternary complexes.

supplementary material, **Fig. S7**), comparable to observations of the binary complex (**Fig. 6 and** electronic supplementary material, **Fig. S7**).

Table 2: Apparent dissociation constants ($K_{d,i}$) for either Chl or S-Et-CoA bound to binary complexes (*Ec*CAT_I:ligand).

	***Ec*CAT$_I$:Chl**	***Ec*CAT$_I$:S-Et-CoA**
$K_{d,1}$	(60 ± 30) μM	(5 ± 2) μM
$K_{d,2}$	(90 ± 40) μM	(10 ± 5) μM
$K_{d,3}$	(130 ± 40) μM	(21 ± 8) μM
$K_{d,intrin}$	(190 ± 90) μM	(14 ± 5) μM
α	0.5	0.8
β	0.2	0.5

Quantification of the K_ds and cooperativity of Chl and S-Et-CoA binding to EcCAT$_I$

Using an ESI-MS ligand-binding method that includes cooperativity parameters [50], approximate dissociation constants (K_d) of gas-phase *Ec*CAT_I bound to Chl or S-Et-CoA, were separately calculated from the data shown in **Figures 4 and 6**. **Table 2** shows the apparent dissociation constants ($K_{d,i}$, where *i* is the number of Chl or S-Et-CoA ligands bound) for sequential addition of Chl or S-Et-CoA with cooperativity constants (α and β). α corresponds to the cooperativity, either positive or negative, of a second ligand of the same type binding to *Ec*CAT_I:1Ligand. β corresponds to the cooperativity of a third ligand of the same type binding to *Ec*CAT_I:2Ligands. $K_{d,1}$ for *Ec*CAT_I:1Chl and *Ec*CAT_I:1S-Et-CoA were (60 ± 30) μM and (5 ± 2) μM, respectively. Interestingly, as the number of bound ligands increases, for both Chl and S-Et-CoA, the apparent $K_{d,i}$ increases (**Table 2**), implying negative cooperativity for binding of either ligand.

DISCUSSION

Herein, we present novel gas-phase structure and stability investigations of trimeric *Ec*CAT_I and several *Ec*CAT_I:ligand complexes. When prepared under native-like conditions, *Ec*CAT_I forms homotrimers with $^{TW}CCS_{N2\rightarrow He}$ values that are comparable to simulated $^{TM}CCS_{He}$ values, which were calculated using crystal structures as models for the native structures, indicating that the biologically relevant homotrimer remains folded in the gas-phase. To further validate the retention of the biologically relevant structure, we observe this gas-phase homotrimer bound to multiple Chl and/or S-Et-CoA ligands. The binding of one, two, or three of either ligand does not affect the protein complexes' arrival time, suggesting that there is not a significant change in its structure upon binding these substrates. This also correlates to crystal structures showing that the ligand-binding sites are at the protein interfaces, buried within the protein [47].

When apo-*Ec*CAT_I is subjected to increasing collision voltage (CV) in CIU experiments, it undergoes two unfolding events before the trimeric species dissociates into unfolded monomers. When *Ec*CAT_I:Chl complexes are

subjected to increasing CV, all Chl molecules dissociate from the complex prior to any *Ec*CAT_I unfolding, revealing that binding of Chl to *Ec*CAT_I does not significantly change the trimeric protein's gas-phase stability.

When incubated with *Ec*CAT_I, a fraction of Ac-CoA was hydrolyzed to CoA, even in the absence of Chl. When Chl is included with *Ec*CAT_I:Ac-CoA, rapid and complete conversion of Ac-CoA to CoA is observed. This high turnover rate did not allow observation of the ternary *Ec*CAT_I:Ac-CoA:Chl complex, likely because of rapid dissociation of the CoA and acetyl-Chl products. Therefore, to trap the reaction in the substrate-bound state, a non-hydrolyzable CoA-derivative, S-Et-CoA, was used. Up to three S-Et-CoA ligands were found coordinating with *Ec*CAT_I. Like Chl, binding of these ligands did not significantly affect the gas-phase structure or stability of *Ec*CAT_I. However, unlike Chl, S-Et-CoA remained bound to *Ec*CAT_I at higher CVs, even as the protein experienced unfolding. While there is no significant difference between the CIU50 values of *Ec*CAT_I and the *Ec*CAT_I:S-Et-CoA complex, the retention of S-Et-CoA at high CV suggests that *Ec*CAT_I binds more tightly to S-Et-CoA than to Chl. This unfolding behavior is supported by our experimental $K_{d,i}$ values, which show that *Ec*CAT_I binds S-Et-CoA more tightly than Chl.

As the ternary complex (*Ec*CAT_I:S-Et-CoA:Chl) is exposed to increasing CV, Chl is released at lower voltages, leaving the more stable *Ec*CAT_I:S-Et-CoA complexes intact. This loss of Chl is consistent with that observed for *Ec*CAT_I:Chl binary complexes, suggesting that the presence of the S-Et-CoA cofactor does not stabilize Chl binding in the ternary complex. Furthermore, the remaining *Ec*CAT_I:S-Et-CoA remains bound even while experiencing protein unfolding at higher CV values. Consistent with observations of the individual binary complexes, binding of both ligands has no significant impact on the gas-phase stability of trimeric *Ec*CAT_I.

The solution-phase K_d for Chl binding to *Ec*CAT_{III} has been reported to be around 4 μM [39]. This value is lower than the experimentally determined gas-phase $K_{d,i}$ for Chl to *Ec*CAT_I of ~60 μM. Gas-phase binding constants often agree with solution-phase binding constants, such as those determined *via* isothermal titration calorimetry using comparable solution conditions [57-59]. Therefore, the differences between these gas-phase $K_{d,i}$ and literature solution-phase K_d could partly be due to the ammonium acetate solvent used for sample preparation compared to the TSE buffer (50 mM Tris-HCl buffer, pH 7.5, containing 100 mM NaCl and 0.1 mM EDTA) used by Ellis *et al.* for their stopped-flow fluorometry experiments [39]. This difference in binding affinity could also be impacted by enzyme differences between *Ec*CAT_I and *Ec*CAT_{III}, where several amino acid substitutions occur in the binding site [47]. Additionally, compared to bulk-phase biochemical assays, native MS has the advantage of quantifying distinct

populations of ligand-bound states simultaneously, whereas typical spectroscopic biochemical techniques suffer from convolution of signals from each species in a bulk solution. This allows us to investigate the cooperativity of sequential ligand binding to *Ec*CAT_I. Interestingly for both Chl and S-Et-CoA, negative cooperativity is observed for the binding of a second and third ligand to *Ec*CAT_I:1Ligand. This observed negative cooperativity suggests that rather than three independent acetylation events to inactivate Chl occurring at all three binding sites simultaneously, sequential inactivation occurs at each site after release of acetylated-Chl from the first binding site.

Using a novel gas-phase approach to quantitively determine *Ec*CAT_I oligomeric protein complex stability and the distribution of ternary complexes formed, we have probed the mechanism of this enzyme to bind and catalytically inactivate Chl. These experiments illustrate the utility of native IMS-MS for the analysis of ternary enzyme complexes and provide a foundation for further characterization of alternative substrates or inhibitors of *Ec*CAT_I. Further, this work highlights how ESI-MS binding experiments can characterize and quantify interactions within protein complexes. Together, the effect of potential Chl derivatives on the gas-phase stability of *Ec*CAT_I and corresponding binding measurements can be executed to model more effective derivatives that are less prone to inactivation and antimicrobial resistance. Similar native MS-based methodology could be applied to new, less toxic derivatives of Chl designed *in silico*, other enzyme systems that have high turnover rates, or to examine entirely different enzyme systems with multivalent-binding mechanisms.

DECLARATIONS

Conflicts of Interests/Completing interests. The authors declare no competing financial interests.

Funding. This work was supported by the following funding agencies: Welch Foundation (AA-1899 to E.S.G.), NSF (CHE-2104242 to M.A.T.), and NIH (1R15GM146188-01).

Acknowledgements. The authors wish to acknowledge the resources and instrumentation in the Molecular Biosciences Center, Mass Spectrometry Center, and the High-Performance Computing Cluster (Kodiak) at Baylor University.

Data availability. All LC-MS/MS raw data have been deposited into the MassIVE data repository with accession number MSV000091635. Data can be downloaded directly via ftp://massive.ucsd.edu/MSV000091635/. Additional data is found in this paper and the associated supporting information.

Electronic Supplementary Material. This article contains supporting information [60-63].

Author Contributions. A.J.B. and M.A.T. were responsible for protein purification. A.N.E and E.S.G. were responsible for design of native MS experiments, while A.N.E. performed the analyses. M.S.C performed the simulations. J.M.C performed the bottom-up proteomics. A.N.E, A.J.B, M.A.T, and E.S.G wrote the manuscript and all authors helped with proofing. All authors have given approval to the final version of the manuscript.

REFERENCES

1. Antimicrobial Resistance C. Global burden of bacterial antimicrobial resistance in 2019: a systematic analysis. Lancet. 2022;399(10325):629-55.
2. Hutchings MI, Truman AW, Wilkinson B. Antibiotics: Past, present and future. Curr Opin Microbiol. 2019;51:72-80.
3. Cook MA, Wright GD. The past, present, and future of antibiotics. Sci Transl Med. 2022;14(657).
4. Ehrlich J, Bartz QR, Smith RM, Joslyn DA, Burkholder PR. Chloromycetin, a New Antibiotic From a Soil Actinomycete. Science. 1947;106(2757):417.
5. Controulis J, Rebstock MC, Crooks HM. Chloramphenicol (Chloromycetin). 5. Synthesis. J Am Chem Soc. 1949;71(7):2463-8.
6. Carter HE, Gottlieb D, Anderson HW. Chloromycetin and Streptothricin. Science. 1948;107(2770):113.
7. Fraunfelder FW, Fraunfelder FT. Scientific challenges in postmarketing surveillance of ocular adverse drug reactions. Am J Ophthalmol. 2007;143(1):145-9.
8. Oong GC, Tadi P. Chloramphenicol. StatPearls. Treasure Island (FL)2022.
9. Khandeparkar P. Reemergence of chloramphenicol in typhoid fever in the era of antibiotic resistance. J Assoc Physicians India. 2010;58 Suppl:45-6.
10. Yunis AA, Miller AM, Salem Z, Arimura GK. Chloramphenicol toxicity: pathogenetic mechanisms and the role of the p-NO2 in aplastic anemia. Clinical toxicology. 1980;17(3):359-73.
11. Drago L. Chloramphenicol Resurrected: A Journey from Antibiotic Resistance in Eye Infections to Biofilm and Ocular Microbiota. Microorganisms. 2019;7(9):278.
12. Dinos GP, Athanassopoulos CM, Missiri DA, Giannopoulou PC, Vlachogiannis IA, Papadopoulos GE, et al. Chloramphenicol Derivatives as Antibacterial and Anticancer Agents: Historic Problems and Current Solutions. Antibiotics. 2016;5(2):20.
13. Dunkle JA, Xiong L, Mankin AS, Cate JH. Structures of the Escherichia coli ribosome with antibiotics bound near the peptidyl transferase center explain spectra of drug action. Proc Natl Acad Sci USA. 2010;107(40):17152-7.
14. Schwarz S, Kehrenberg C, Doublet B, Cloeckaert A. Molecular basis of bacterial resistance to chloramphenicol and florfenicol. FEMS microbiology reviews. 2004;28(5):519-42.
15. Lewendon A, Shaw WV. Transition state stabilization by chloramphenicol acetyltransferase. Role of a water molecule bound to threonine 174. J Biol Chem. 1993;268(28):20997-1001.
16. Shaw WV. The enzymatic acetylation of chloramphenicol by extracts of R factor-resistant Escherichia coli. J Biol Chem. 1967;242(4):687-93.
17. Kleanthous C, Shaw WV. Analysis of the mechanism of chloramphenicol acetyltransferase by steady-state kinetics. Evidence for a ternary-complex mechanism. The Biochemical journal. 1984;223(1):211-20.
18. Thibault G, Guitard M, Daigneault R. A study of the enzymatic inactivation of chloramphenicol by highly purified chloramphenicol acetyltransferase. Biochim Biophys Acta. 1980;614(2):339-42.

19. Rodriguez GM, Tashiro Y, Atsumi S. Expanding ester biosynthesis in Escherichia coli. Nat Chem Biol. 2014;10(4):259-65.
20. Alonso-Gutierrez J, Chan R, Batth TS, Adams PD, Keasling JD, Petzold CJ, et al. Metabolic engineering of *Escherichia coli* for limonene and perillyl alcohol production. Metab Eng. 2013;19:33-41.
21. Seo H, Lee JW, Giannone RJ, Dunlap NJ, Trinh CT. Engineering promiscuity of chloramphenicol acetyltransferase for microbial designer ester biosynthesis. Metab Eng. 2021;66:179-90.
22. Murray IA, Shaw WV. O-Acetyltransferases for chloramphenicol and other natural products. Antimicrob Agents Chemother. 1997;41(1):1-6.
23. Day PJ, Murray IA, Shaw WV. Properties of hybrid active sites in oligomeric proteins: kinetic and ligand binding studies with chloramphenicol acetyltransferase trimers. Biochemistry. 1995;34(19):6416-22.
24. Leslie AG, Moody PC, Shaw WV. Structure of chloramphenicol acetyltransferase at 1.75-A resolution. Proc Natl Acad Sci USA. 1988;85(12):4133-7.
25. VanderSchueren J, Robben J, Goossens K, Heremans K, Volckaert G. Identification of local carboxy-terminal hydrophobic interactions essential for folding or stability of chloramphenicol acetyltransferase. J Mol Biol. 1996;256(5):878-88.
26. Li WM, Ruf S, Bock R. Chloramphenicol acetyltransferase as selectable marker for plastid transformation. Plant Mol Biol. 2011;76(3-5):443-51.
27. Cubrilovic D, Barylyuk K, Hofmann D, Walczak MJ, Graber M, Berg T, et al. Direct monitoring of protein-protein inhibition using nano electrospray ionization mass spectrometry. Chem Sci. 2014;5(7):2794-803.
28. Hannah VV, Atmanene C, Zeyer D, Van Dorsselaer A, Sanglier-Cianferani S. Native MS: An 'ESI' way to support structure- and fragment-based drug discovery. Future Med Chem. 2010;2(1):35-50.
29. Blackwell AE, Dodds ED, Bandarian V, Wysocki VH. Revealing the quaternary structure of a heterogeneous noncovalent protein complex through surface-induced dissociation. Anal Chem. 2011;83(8):2862-5.
30. Norris A, Busch F, Schupfner M, Sterner R, Wysocki VH. Quaternary structure of the tryptophan synthase alpha-subunit homolog BX1 from *Zea mays*. J Am Soc Mass Spectrom. 2020;31(2):227-33.
31. Barth M, Schmidt C. Native mass spectrometry-A valuable tool in structural biology. J Mass Spectrom. 2020;55(10):e4578.
32. Leney AC, Heck AJ. Native Mass Spectrometry: What is in the Name? J Am Soc Mass Spectrom. 2017;28(1):5-13.
33. Moreno-Pedraza A, Rosas-Roman I, Garcia-Rojas NS, Guillen-Alonso H, Ovando-Vazquez C, Diaz-Ramirez D, et al. Elucidating the distribution of plant metabolites from native tissues with laser desorption low-temperature plasma mass spectrometry imaging. Anal Chem. 2019;91(4):2734-43.
34. Nguyen GTH, Tran TN, Podgorski MN, Bell SG, Supuran CT, Donald WA. Nanoscale ion emitters in native mass spectrometry for measuring ligand-protein binding affinities. ACS Cent Sci. 2019;5(2):308-18.
35. Ahdash Z, Lau AM, Martens C, Politis A. Analyzing protein architectures and protein-ligand complexes by integrative structural mass spectrometry. J Vis Exp. 2018(140).
36. Hopper JT, Oldham NJ. Collision induced unfolding of protein ions in the gas phase studied by ion mobility-mass spectrometry: the effect of ligand binding on conformational stability. J Am Soc Mass Spectrom. 2009;20(10):1851-8.
37. Eschweiler JD, Rabuck-Gibbons JN, Tian Y, Ruotolo BT. CIUSuite: A Quantitative Analysis Package for Collision Induced Unfolding Measurements of Gas-Phase Protein Ions. Anal Chem. 2015;87(22):11516-22.
38. Polasky DA, Dixit SM, Fantin SM, Ruotolo BT. CIUSuite 2: Next-Generation Software for the Analysis of Gas-Phase Protein Unfolding Data. Anal Chem. 2019;91(4):3147-55.
39. Ellis J, Bagshaw CR, Shaw WV. Substrate binding to chloramphenicol acetyltransferase: evidence for negative cooperativity from equilibrium and kinetic constants for binary and ternary complexes. Biochemistry. 1991;30(44):10806-13.
40. Gabelica V, Shvartsburg AA, Afonso C, Barran P, Benesch JLP, Bleiholder C, et al. Recommendations for reporting ion mobility Mass Spectrometry measurements. Mass Spectrom Rev. 2019;38(3):291-320.
41. Ruotolo BT, Benesch JLP, Sandercock AM, Hyung S-J, Robinson CV. Ion mobility–mass spectrometry analysis of large protein complexes. Nat Protoc. 2008;3(7):1139-52.
42. Edwards AN, Tran HM, Gallagher ES. Propagating Error through Traveling-Wave Ion Mobility Calibration. J Am Soc Mass Spectrom. 2021;32(11):2621-30.
43. Phetsanthad A, Li G, Jeon CK, Ruotolo BT, Li L. Comparing Selected-Ion Collision Induced Unfolding with All Ion Unfolding Methods for Comprehensive Protein Conformational Characterization. J Am Soc Mass Spectrom. 2022;33(6):944-51.
44. GROMACS 2022.3 Manual (2022.3) [Internet]. 2022.

45. Huang J, MacKerell AD, Jr. CHARMM36 all-atom additive protein force field: validation based on comparison to NMR data. J Comput Chem. 2013;34(25):2135-45.
46. Rolland AD, Prell JS. Computational Insights into Compaction of Gas-Phase Protein and Protein Complex Ions in Native Ion Mobility-Mass Spectrometry. TrAC, Trends Anal Chem. 2019;116:282-91.
47. Biswas T, Houghton JL, Garneau-Tsodikova S, Tsodikov OV. The structural basis for substrate versatility of chloramphenicol acetyltransferase CATI. Protein Sci. 2012;21(4):520-30.
48. Ewing SA, Donor MT, Wilson JW, Prell JS. Collidoscope: An Improved Tool for Computing Collisional Cross-Sections with the Trajectory Method. J Am Soc Mass Spectrom. 2017;28(4):587-96.
49. Mesleh MF, Hunter JM, Shvartsburg AA, Schatz GC, Jarrold MF. Structural Information from Ion Mobility Measurements: Effects of the Long-Range Potential. J Phys Chem A. 1996;100(40):16082-6.
50. Baez Bolivar EG, Bui DT, Kitova EN, Han L, Zheng RB, Luber EJ, et al. Submicron Emitters Enable Reliable Quantification of Weak Protein-Glycan Interactions by ESI-MS. Anal Chem. 2021;93(9):4231-9.
51. Shaw WV, Leslie AG. Chloramphenicol acetyltransferase. Annu Rev Biophys Biophys Chem. 1991;20(1):363-86.
52. Shaw WV, Packman LC, Burleigh BD, Dell A, Morris HR, Hartley BS. Primary structure of a chloramphenicol acetyltransferase specified by R plasmids. Nature. 1979;282(5741):870-2.
53. Murray IA, Martinez-Suarez JV, Close TJ, Shaw WV. Nucleotide sequences of genes encoding the type II chloramphenicol acetyltransferases of Escherichia coli and Haemophilus influenzae, which are sensitive to inhibition by thiol-reactive reagents. The Biochemical journal. 1990;272(2):505-10.
54. Murray IA, Hawkins AR, Keyte JW, Shaw WV. Nucleotide sequence analysis and overexpression of the gene encoding a type III chloramphenicol acetyltransferase. The Biochemical journal. 1988;252(1):173-9.
55. Chan DS, Kavanagh ME, McLean KJ, Munro AW, Matak-Vinkovic D, Coyne AG, et al. Effect of DMSO on Protein Structure and Interactions Assessed by Collision-Induced Dissociation and Unfolding. Anal Chem. 2017;89(18):9976-83.
56. Park JJ, Han SY. Alternated Branching Ratios by Anomaly in Collision-Induced Dissociation of Proton-Bound Hoogsteen Base Pairs of 1-Methylcytosine with 1-Methylguanine and 9-Methylguanine. J Am Soc Mass Spectrom. 2019;30(5):846-54.
57. Wang W, Kitova EN, Klassen JS. Influence of solution and gas phase processes on protein-carbohydrate binding affinities determined by nanoelectrospray Fourier transform ion cyclotron resonance mass spectrometry. Anal Chem. 2003;75(19):4945-55.
58. Yao Y, Shams-Ud-Doha K, Daneshfar R, Kitova EN, Klassen JS. Quantifying protein-carbohydrate interactions using liquid sample desorption electrospray ionization mass spectrometry. J Am Soc Mass Spectrom. 2015;26(1):98-106.
59. Gulbakan B, Barylyuk K, Schneider P, Pillong M, Schneider G, Zenobi R. Native Electrospray Ionization Mass Spectrometry Reveals Multiple Facets of Aptamer-Ligand Interactions: From Mechanism to Binding Constants. J Am Chem Soc. 2018;140(24):7486-97.
60. Johnston HE, Yadav K, Kirkpatrick JM, Biggs GS, Oxley D, Kramer HB, et al. Solvent Precipitation SP3 (SP4) Enhances Recovery for Proteomics Sample Preparation without Magnetic Beads. Anal Chem. 2022;94(29):10320-8.
61. Li D, Farchone A, Zhu Q, Macchi F, Walker DE, Michels DA, et al. Fast, Robust, and Sensitive Identification of Residual Host Cell Proteins in Recombinant Monoclonal Antibodies Using Sodium Deoxycholate Assisted Digestion. Anal Chem. 2020;92(17):11888-94.
62. Bern M, Kil YJ, Becker C. Byonic: advanced peptide and protein identification software. Curr Protoc Bioinformatics. 2012;Chapter 13:13 20 1-13 20 14.
63. UniProt C. UniProt: the Universal Protein Knowledgebase in 2023. Nucleic Acids Res. 2023;51(D1):D523-D31.